Composites Science and Technology 143 (2017) 56–66

Contents lists available at ScienceDirect

Composites Science and Technology

journal homepage: http://www.elsevier.com/locate/compscitech

Conductive carboxylated styrene butadiene rubber composites by incorporation of polypyrrole-wrapped halloysite nanotubes

Yongwang Liu, Mingxian Liu*

Department of Materials Science and Engineering, Jinan University, Guangzhou, 510632, PR China

ARTICLE INFO

Article history:
Received 7 December 2016
Received in revised form
19 February 2017
Accepted 1 March 2017
Available online 2 March 2017

Keywords:
Halloysite
Polypyrrole
Composite
Conductive
Mechanical property

ABSTRACT

Polypyrrole-wrapped halloysite nanotubes (PPy@HNTs) are prepared by polymerization of pyrrole on the surfaces of HNTs. PPy@HNTs show improved dispersion ability and stability in water compared with pure PPy due to the increased zeta potential. The PPy@HNTs dispersions are compounded with carboxylated styrene-butadiene rubber (xSBR) latex to prepare conductive xSBR/PPy@HNTs composites. The morphology, conductive performance, mechanical properties, and swelling performance of the xSBR/PPy@HNTs composites are determined. PPy@HNTs can be uniformly dispersed in the rubber matrix and form a conductive network. The conductivity of the composites increases with the loading of PPy@HNTs. When the content of PPy@HNTs is 10%, the conductivity of the xSBR rubber increases to 1.82×10^{-4} s/m which is much higher than the corresponding xSBR/neat PPy composites (4.62×10^{-8} s/m). Also, the composites show significantly improved mechanical properties both in static and dynamic condition. The tensile strength, Young's modulus, and storage modulus of the composites are substantially higher than those of pure xSBR. The rigid filler networks effectively limit the mobility of rubber molecule chains, which leads to decreased water swelling capacity and crosslink density. The prepared high performance rubber composites with good conductivity show promising applications in many areas such as piezoresistive sensor.

1. Introduction

In recent years, conductive polymer material becomes a popular research field since these materials have shown many promising applications such as electromagnetic interference shielding, biosensor and chemical sensors, electrolytic capacitors, polymer electrode, organic light emitting diodes, and plastic solar cells [1–3]. The commonly used conductive polymers include polypyrrole (PPy), polythiophene, and polyanilines [4–8]. PPy is a kind of heterocyclic conjugated conducting polymers, usually in the form of amorphous black solid. PPy is obtained by polymerization of pyrrole monomers via chemical or electrochemical means. Chemical synthesis involves mixing a strong oxidizing agent (typically $FeCl_3$) with a pyrrole monomer aqueous solution, so this routine is preferred for research purposes due to the simplicity of the technique [9,10]. The conductivity and stability of PPy powder produced by means of chemical oxidation polymerization were substantially improved. However, the practical application of PPy powder remained problematic due to the difficulty of processing arising from their poor dispersion ability [11]. PPy can form a continuous film or coating on the surfaces of many types of nanoparticles by the in situ polymerization method, which leads to a hybrid conductive filler for polymer composites [12]. For example, uniform MnO_2/PPy multifunctional nanocoatings with thickness of ~20 nm can be formed on individual electrospun carbon nanofibers (CNFs), which constructing a high-performance supercapacitor [13]. PPy can also coat on the electrospinned poly-L-lactic acid nanofibrous scaffold via in situ surface polymerization, which shows improved cell growth and shows potential applications in the nerve tissue engineering as cells substrate to apply electrical stimulation [14]. Recently, Zhang et al. compounded PPy supported cellulose nanowhiskers with natural rubber (NR) latex, and the resulting rubber composite exhibited significant improvement in electrical conductivity and mechanical properties when compared with neat PPy/NR composites [15,16].

Halloysite is a kind of silicate minerals, which are abundant in nature, mainly in the form of nanotubes morphology [17,18]. Halloysite nanotubes (HNTs) are formed by curling of kaolin sheets and the layer numbers is more than twenty. The inner diameter, outer

* Corresponding author.
E-mail address: liumx@jnu.edu.cn (M. Liu).

http://dx.doi.org/10.1016/j.compscitech.2017.03.001
0266-3538/

diameter, and length of HNTs is in the range of 15–20 nm, 50–70 nm, and 100–1500 nm, respectively [19,20]. The chemical formula of HNTs is $Al_2Si_2O_4(OH)_4 \cdot nH_2O$, where $n = 2$ and 0 represent hydrous HNTs and anhydrous HNTs (layer spacing are 10 and 7 Å, respectively) [21]. The lamellae of HNTs are composed of outer silica and the inner layer of aluminum oxide octahedral regular arrangement, while the middle layer is adsorbed water molecules. The elastic modulus of single HNTs is about 130 GPa with a certain toughness, so HNTs combine the advantages of high aspect ratio, large surface area, high strength, good dispersion capacity, easily chemical modification, naturally available, and environmental/biological compatibility as polymer fillers [22–25]. HNTs can be mixed with polymers both in solution or melt state for forming high performance polymer composites [26]. The mechanical properties, thermal properties, flame retardance properties, cytocompatibility of polymers can be significantly increased by the incorporation of HNTs [27,28]. HNTs with good dispersity enable the formation of filler networks in polymer matrix, which is corresponding for the mechanical performance improvement and dimensional stability under heat [29,30]. Inspired these results, if one coating the HNTs with conductive polymers effectively, then a 3D hierarchical multiscale conductive networks can be formed in polymer matrix and a conductive polymer composite can be prepared. Previous study also showed that the surfaces of HNTs are composed of siloxane and hydroxyl groups which could provide active sites for the polymerization of the pyrrole on the surfaces of the nanotubes [31].

Carboxylated styrene-butadiene rubber (xSBR) is a copolymer of styrene, butadiene and a small amount of acrylic acid, which combines the advantages of high adhesion and conjunctival strength, mechanical and chemical stability, high mobility, and storage stability. Due to the introduction of carboxyl groups, the polarity of the xSBR latex is increased and the adhesive properties are improved. The common application area of xSBR includes the papermaking, carpets, textiles, jewelry, modified cement mortar, wood glue, modified asphalt, oil drilling, and so on [32].

In this study, PPy-wrapped HNTs (PPy@HNTs) was synthesized in situ chemical oxidation polymerization of pyrrole in the HNTs aqueous dispersion. The PPy@HNTs hybrids showed excellent suspension stability in water due to the high surface charge, which facilitated the uniformly dispersion of PPy@HNTs in xSBR latex. The morphology, mechanical, conductive, and swelling properties of the xSBR/PPy@HNTs conductive composites were then investigated in detail. Compared with carbon nanotubes and other metal nanotubes, the dispersion of PPy@HNTs in the polar solvents and the subsequently in rubber is good without adding any stabilizer. They can also effectively form a continuous conductive network in the rubber matrix, which leads to a high-performance conductive rubber. The present work a simple and easily scale-up strategy for synthesis of high-performance conductive rubber composites using natural tubular nanoparticles as template of conductive polymer, which shows promising applications in conductive composite such as piezoresistive sensor, polymer electrodes and capacitors.

2. Experimental

2.1. Materials

Halloysite nanotubes (HNTs) were purchased from Guangzhou Runwo Materials Technology Co., Ltd., China. Ferric chloride ($FeCl_3$) (analytical grade) was purchased from Guangzhou chemical reagent factory. Pyrrole (Py) monomer was purchased from Sigma-Aldrich. Carboxylated styrene butadiene rubber (xSBR) with solids content of 50 wt% was purchased from Guangzhou Juntai Materials Co. Ltd. (China). Other chemicals used in this study were of analytical grade and used as received. Water was purified by deionization and filtration with a Millipore purification apparatus (resistivity > 18.2 MΩ cm).

2.2. Preparation of xSBR/PPy@HNTs composite films

PPy@HNTs were synthesized according to previous study with slight modification [15]. The typical synthesis procedure was introduced below. 2 g of HNTs powder was suspended in 200 mL of distilled water and ultrasonically treated for 30 min to get homogenous dispersion. Then 2 mL pyrrole monomer (0.03 mol) was added into the HNTs dispersion under stirring in ice–water mixture. After 1 h, 4 g $FeCl_3 \cdot 6H_2O$ (0.015 mol) was added into the mixture as catalyst. The pyrrole was polymerized on the surfaces of HNTs for 4 h, which leaded to the formation of a layer of continuous conductive layer. The resulting dispersion was subjected to centrifugation and washed using pure water for three times. Afterwards, PPy@HNTs solid powder was obtained by freeze-drying at −80 °C. Neat PPy was synthesized under the same conditions but without the addition of HNTs.

xSBR/PPy@HNTs composite films were prepared via solution mixing and casting drying method. A certain amount of PPy@HNTs powder was dispersed into xSBR latex under stirring for at least 5 h to obtain a homogenous mixture. The xSBR/PPy@HNTs composite films were obtained by oven drying at 60 °C for 16 h in a square PTFE mold (10 cm × 10 cm). The synthesis of PPy@HNTs and the preparation process of the xSBR/PPy@HNTs conductive composites were schematically illustrated in Fig. 1. The composites were denoted by the weight percent of the PPy@HNTs relative to the xSBR.

2.3. Characterizations

2.3.1. ξ-potential and particle size analysis

The ξ-potential and particle size distribution of HNTs, PPy, and PPy@HNTs aqueous dispersions were measured using a Zetasizer Nano ZS. The concentration of the dispersion was 1×10^{-3} wt%. Before determination, the samples were subjected into ultrasonic treatment for 30 min at 570 W.

2.3.2. Transmission electron microscopy (TEM)

0.05 wt% of HNTs and PPy@HNTs aqueous dispersions were dropped in carbon membrane supported copper mesh and dried naturally, then the samples were observed on Tecnai Philips 10 TEM at an accelerating voltage of 100 kV.

2.3.3. Fourier transform infrared spectroscopy (FTIR)

FTIR spectra were measured by infrared spectroscopy using attenuated total reflection (ATR) model in a NICOLET iS10 FT-IR Spectrometer. Thirty-two consecutive experiments were performed and averaged. The spectral scope ranged from 4000 to 400 cm^{-1} with a wavenumber resolution of 2 cm^{-1}.

2.3.4. X-ray diffraction (XRD)

XRD patterns of HNTs, neat xSBR, and xSBR/PPy@HNTs composite films were determined by X-ray diffraction (Rigaku, Miniflex600, CuK_α, Japan) at an accelerating voltage of 40 kV and the current of 40 mA.

2.3.5. Scanning electron microscopy (SEM)

The composite films were broken in liquid nitrogen and the cryofractured surface of the composites films was observed by ZEISS, Ultra 55 SEM. Before the observation, a thin gold layer was sprayed on the sample surfaces.

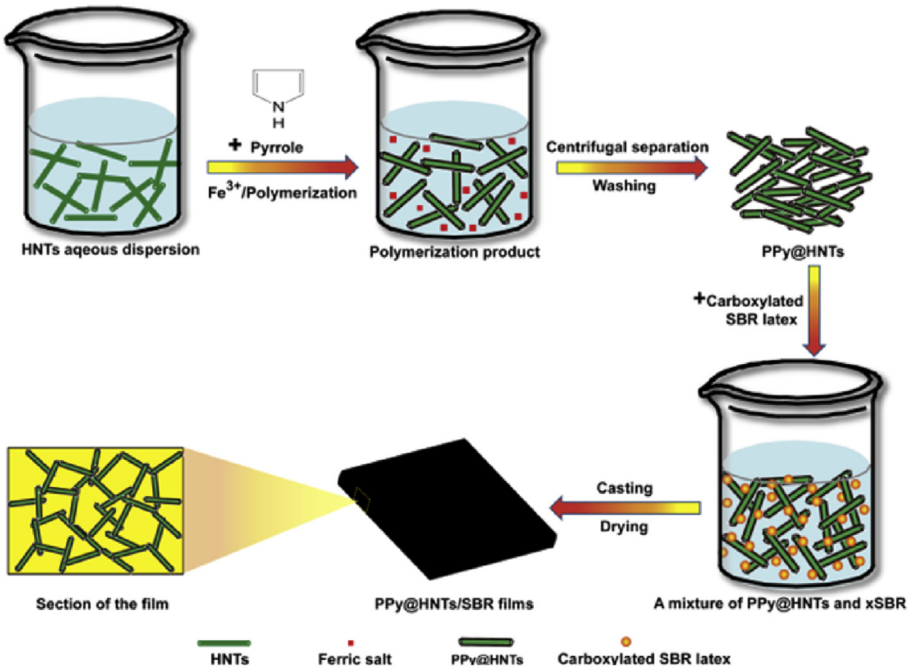

Fig. 1. Schematic illustration for the synthesis of PPy@HNTs and the preparation process of the xSBR/PPy@HNTs conductive composites.

2.3.6. Electrical conductivity determination

The conductivity of the rubber samples was measured by two-point measurement with a high resistance instrument (ZC36, for $R > 2 \times 10^8\ \Omega$) and a multimeter (Fluke 17B$^+$, for $R \leq 2 \times 10^8\ \Omega$).

2.3.7. Mechanical properties determination

The neat xSBR and composite films were firstly cut into the dumbbell shape with width and thickness of 6 mm × 0.3 mm. Universal testing machine (U-CAN UT-2060, Taiwan) was used to determine the tensile properties at a strain rate of 5 mm/min. The stress-strain curves of the samples were recorded. The tensile modulus at 100%, 300%, and 500% was the stress required to stretch the sample to 100%, 300%, or 500% elongation (strain).

2.3.8. Dynamic mechanical analysis (DMA)

DMA experiment was carried out by TA Q800 in a tensile mode at oscillation frequency of 1.0 Hz and from −100 to 100 °C with heating rate of 3 °C/min. The experiments were conducted under nitrogen atmosphere.

2.3.9. Differential scanning calorimetry (DSC)

DSC measurements were carried out on a TAQ20 analyzer (TA Instruments, USA). The experiment was conducted at a temperature range of −90 to 100 °C with heating rate of 10 °C/min using nitrogen as purging gas. To evaluate the amount of immobilized rubber around the particles in the composite, the value of the heat capacity step ΔC_{pn} which is proportional to the internal degree of freedom of molecular motion was calculated by DSC result. From the ΔC_{pn} value, the weight fraction of the immobilized polymer layer χ_{im} could be obtained. ΔC_{pn} and χ_{im} were calculated as follows:

$$\Delta C_{pn} = \frac{\Delta C_p}{(1-w)}$$

$$\chi_{im} = \frac{\Delta C_{p0} - \Delta C_{pn}}{\Delta} C_{p0}$$

here, ΔC_p is the heat capacity jump at T_g (0–20 °C in the present systems) which can be calculated by TAQ20 analyzer software. w is the weight fraction of filler. ΔC_{pn} is normalized to the polymer weight fraction. ΔC_{p0} referrers to the heat capacity jump at T_g of the unfilled polymer matrix. χ_{im} is the weight fraction of the immobilized polymer layer.

2.3.10. Thermogravimetric analysis (TGA)

TGA curves of raw HNTs, PPy@HNTs, neat xSBR and xSBR/PPy@HNTs composites films were tested using the NETZSCHTG 209 F3 Tarsus under a nitrogen atmosphere from room temperature to 750 or 600 °C at a heating rate of 10 °C/min.

2.3.11. Swelling behavior in water

The water absorption was compared by the weighting the samples at dry state and after immersion in pure water for 3 days at room temperature. The swelling ratio is calculated according to the following formula.

$$\text{swelling ratio} = \frac{\text{mass of wet sample} - \text{mass of dry sample}}{\text{mass of dry sample}} \times 100\%$$

2.3.12. Crosslink density measurements

Crosslink density of the samples was determined by equilibrium swelling method using toluene. For the test, the rubber samples were cut into thin pieces with same size and weighed (m_0). The samples were soaked in toluene for 3 days at room temperature under shaking with a rate of 100 rpm. Then the samples were taken

out from toluene and weighted (m_1). Then the samples were dried at 60 °C for 12 h and weighted again (m_2). The volume fraction of the xSBR swelled state (V_r) is calculated by the following Flory-Rhener equation [33].

$$V_r = \frac{m_0 \times \Phi \times \frac{(1-\alpha)}{\rho_r}}{m_0 \times \Phi \times \frac{1-\alpha}{\rho_r} + \frac{(m_1-m_2)}{\rho_s}}$$

Φ is the rubber mass fraction of the composite, α is the mass loss of the composite during the swelling process, ρ_r and ρ_s are the density of the rubber and the solvent, respectively.

The crosslinking density of composite (V_e) was calculated according to the following formula [34].

$$V_e = -\frac{\ln(1-V_r) + V_r + \chi V_r^2}{V_s(\sqrt{3}V_r - V_r/2)}$$

V_s is the molar volume of the solvent (toluene is 107 cm^3/mol), χ is the interaction parameter of xSBR-toluene (0.00653).

3. Results and discussion

3.1. Characterization of PPy@HNTs

HNTs have good dispersion ability in water due to the repulsion effect arise from their high surface negative charge, which can be employed to prepare water-soluble polymers composite. Fig. 2 shows the appearance of the HNTs aqueous dispersion, PPy aqueous dispersion, and PPy@HNTs dispersion at 0 h and after 24 h. It is clear that both HNTs and PPy@HNTs dispersion are stable for 24 h without sedimentation. In contrast, the PPy dispersion exhibits significant sedimentation after standing 24 h. This suggests that HNTs can increase the dispersion ability of PPy in the water. The ζ-potential values of HNTs, PPy, and PPy@HNTs dispersions are shown in Fig. 2(A). The ζ-potential of HNTs dispersion is −27.4 mV, so HNTs dispersion is stable after standing 24 h. PPy is a positively charged conducting polymer, and the ζ-potential of PPy dispersion is determined as +16.4 mV. After 24 h of standing, PPy is settled down at the bottom of bottle, indicating that the stability of neat PPy in water is poor. The aggregated PPy can lead to a decreased of the conductive efficacy when using as filler in polymer matrix. The ζ-potential of PPy@HNTs dispersion is +24.0 mV, and PPy@HNTs show high stability in water without any precipitate after standing for 24 h. Beside the increased ζ-potential, the hydrophilicity and the small dimensions of HNTs also contribute the dispersion stability of the PPy@HNTs in water [35]. Therefore, PPy@HNTs will be uniformly dispersed in the xSBR latex to obtain homogenous conductive xSBR/PPy@HNTs composites. The morphology and particle size distribution of PPy@HNTs were further investigated. As shown in Fig. 2(B), HNTs show an empty tube-like morphology with aspect ratio in 8–25. All the tubes show smooth and sharp outer surface. In contrast, PPy@HNTs have different appearances with pristine HNTs. The outer surface of the HNTs is covered with a layer of polymer film in the PPy@HNTs sample, suggesting the warping of PPy on HNTs with continuous conductive layer. Also, it can be seen the tubes in the PPy@HNTs can link each other and form a continuous network due to the interactions among the tubes. The particle size distributions of HNTs and PPy@HNTs are then determined by laser particle size analyzer. From Fig. 2(C), HNTs and PPy@HNTs show that the average size is 369.9 ± 16.3 nm and 530.4 ± 16.8 nm, respectively. The slightly increased size of PPy@HNTs is attributed to the partly crosslinking of HNTs by the PPy. The formation of conductive network structure of PPy@HNTs in rubber matrix is then expected. TGA curves of HNTs and PPy@HNTs are shown in Fig. 2(D). The curves show that the residual of PPy@HNTs is less than that of raw HNTs, which is due to the degradation of the PPy wrapped on the surface of HNTs. The PPy content in the PPy@HNTs nanohybrids is calculated as 5.31% from the TGA result.

FTIR analysis was carried out to study the chemical structures of HNTs, PPy, and PPy@HNTs composites. As shown in Fig. 3, HNTs' characteristic bands appear at 3695 and 3622 cm^{-1}, which are attributed to the O–H stretching of inner-surface hydroxyl groups and inner hydroxyl groups, respectively [36]. The characteristic bands of PPy at 1543 and 1453 cm^{-1} are assigned to stretching vibration of pyrrole ring, and the bands at 1300 and 1165 cm^{-1} are ascribed to the deforming vibration of C–H (together with N–H) and stretching of C–N, respectively [15,37]. The bands at 1040, 905, and 780 cm^{-1} are assigned to C–C stretching vibration, C–H out-of-plane vibration, and C–H wagging vibrations, respectively. The PPy@HNTs show the characteristics peaks for both HNTs and PPy. Due to the hydrogen bonding interactions of PPy with HNTs, the characteristic bands of PPy at 1543, 1165, and 1040 cm^{-1} shift towards high wavenumber. Similar up-shiftiest of PPy bands due to the interfacial interactions have also been found in other literature [38]. All these results suggest that pyrrole monomer is successfully polymerized on the surfaces of HNTs and the warping of PPy on HNTs increases the dispersion ability in aqueous media.

3.2. Structure of the xSBR/PPy@HNTs composites

FTIR spectra of xSBR and xSBR/PPy@HNTs composites are shown in Fig. 4(a). The spectra of xSBR shows peaks at 697 cm^{-1} due to styrene units, 757 cm^{-1} due to 1,4 cis, 909 cm^{-1} due to 1,2 vinyl and 967 cm^{-1} due to 1,4 trans butadiene units [39]. The peaks around 1650 cm^{-1} are assigned to the C=C group, 3100-2800 cm^{-1} is assigned to the stretching vibration of C–H group, 1451 and 1493 cm^{-1} are assigned to the stretching vibration of C–C in the benzene ring. After incorporation of PPy@HNTs, the composites show the peaks of both xSBR and HNTs. For example, the peaks around 1072 and 1026 cm^{-1} assigned to the in-plane Si–O stretching of HNTs gradually increase in the spectra of the composite with the loading of the PPy@HNTs. Meanwhile, the intensity of peaks assigned to xSBR decreases in the composites.

Fig. 4(b) shows the XRD patterns of xSBR and xSBR/PPy@HNTs composites. It can be seen the neat xSBR exhibits a wide diffraction peak at $2\theta = 20°$, which indicates that the rubber matrix is in amorphous state. The XRD patterns of HNTs show strong diffraction peaks of 2θ at 12°, 20°, and 25°, which is attributed to the (001) plane, (020,110) plane, and (002) plane. When the content of PPy@HNTs in the composite is less than 2.5 wt%, no characteristic peaks of HNTs can be identified in the XRD patterns of the composites. When the content of PPy@HNTs is more than 2.5 wt%, the composites gradually shows diffraction peaks of HNTs in the corresponding location. The peak at $2\theta = 12°$ shift to higher 2θ value in the rubber composite, indicating the layer spacing of HNTs decreases. This may due to the interfacial interactions between PPy@HNTs and the xSBR rubber chains, which leads to loss of the adsorbed water molecules in the layers of HNTs. It also should be noted that a small diffraction peak around 18° is attributed to the impurities of HNTs [40]. X-ray diffraction results show that PPy@HNTs is successfully incorporated into the xSBR matrix.

In order to study the dispersion state of PPy@HNTs in the rubber matrix, SEM experiment of neat xSBR and xSBR/PPy@HNTs composites was conducted (Fig. 5). For the neat xSBR, the cross section of the rubber is quite clear and smooth. In contrast, white spots and rod-like substance appear in the SEM image of xSBR/PPy@HNTs composites. These represent the PPy@HNTs in the rubber composite. With the increase in loading of PPy@HNTs, more and more

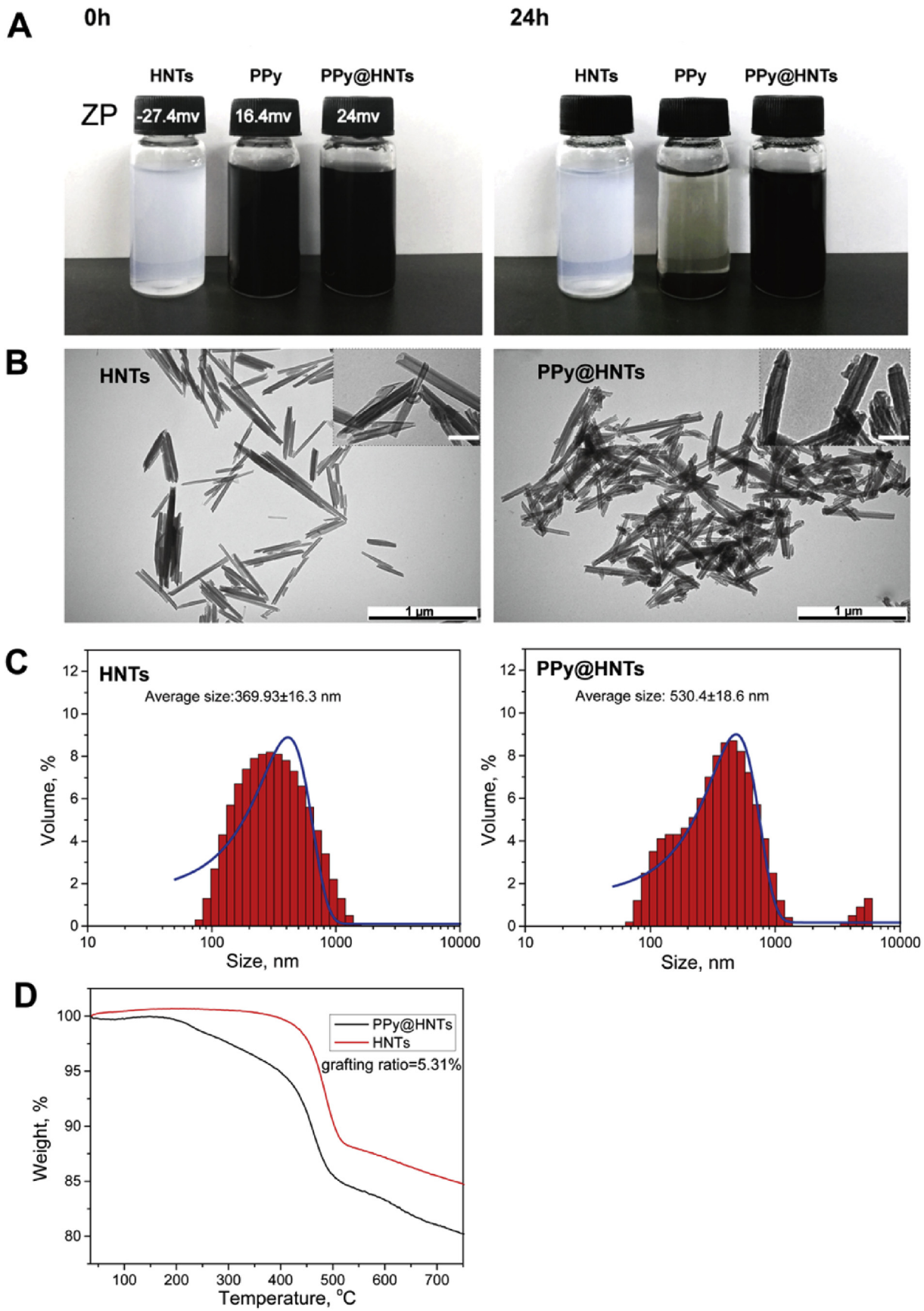

Fig. 2. Appearance and the ζ-potential values of HNTs, PPy, and PPy@HNTs in water before and after standing for 24 h (A); TEM image of HNTs and PPy@HNTs (the inset show the TEM images at higher magnification, scale bar = 100 nm) (B); Size distribution in aqueous dispersion (C) and TGA curves of HNTs and PPy@HNTs (D).

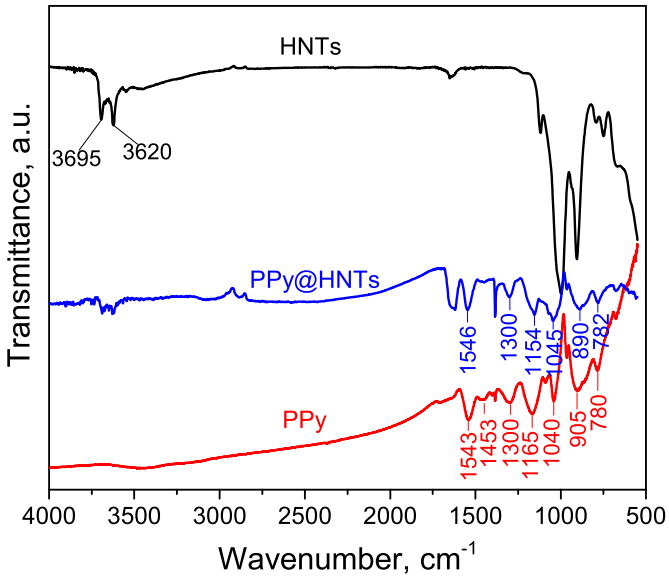

Fig. 3. FTIR spectra of HNTs, PPy, and PPy@HNTs.

PPy@HNTs can be observed in the matrix. PPy@HNTs can be uniformly dispersed in the rubber matrix and nearly no aggregates of PPy@HNTs can be found. After carefully checking the images, one can see the interfaces of HNTs and the rubber is blurry, which suggests the good interfacial bonding in the composite. Due to the high aspect ratio of HNTs and the interactions among the tubes, the PPy@HNTs can form continuous conductive network in the rubber matrix especially at high loading. As a consequence, both the mechanical and conductivity of the composites are enhanced. The formation of the continuous filler network can also be evidenced by the appearance of the rubber composite (uniform black without filler aggregates). Although one can not directly observe the 3D network of the PPy@HNTs in the rubber matrix from SEM images, the conductivity determination of the composites in the following section confirms the formation of continuous conductive network. All these results demonstrate that PPy@HNTs are successfully incorporated into the xSBR matrix and can be dispersed evenly with good interfacial interactions with the xSBR.

3.3. Conductive properties of the xSBR/PPy@HNTs composites

PPy can form a continuous film or coating on the surfaces of many types of nanoparticles by the in situ polymerization method, which leads to a hybrid conductive filler for polymer composites. The conductivity of xSBR/PPy@HNTs and xSBR/PPy composites with different filler content was compared in Fig. 6. Neat xSBR is an insulator with conductivity less than 10^{-9} s/m. With the increase of the content of PPy@HNTs filler, the conductivity of the composites gradually increased. When the content of filler is 2.5 wt% (the corresponding content of PPy is 0.06%), the conductivity of the sample increased from 5.27×10^{-11} s/m to 2.68×10^{-7} s/m. The maximum conductivity of the composite is 1.82×10^{-4} s/m which is corresponding the composite with 10 wt% PPy@HNTs content. This is due to the fact that the PPy@HNTs can form a continuous conductive network in the rubber matrix. In contrast, neat PPy can not be uniformly dispersed in xSBR matrix, so the conductivity of xSBR/PPy composites is poor. We also prepared xSBR/PPy/HNTs (100/0.27/5) ternary composites, however, the composites showed a relatively low conductivity ($<10^{-8}$ s/m) and mechanical property. The conductivity of the xSBR/PPy@HNTs composites with 10 wt% filler content is superior for the natural rubber (NR)/PPy@cellulose nanowhisker (CNCs) systems. In the NR/PPy@CNCs composite with 10% filler content, the conductivity is only 2.5×10^{-9} s/m [15]. The conductivity of the prepared composites is comparable with that of NR/PPy/layered silicates (Na^{+}-MMT) composites [41]. The xSBR/PPy@HNTs composites with 10 wt% filler content was cut into a small strip to determine their conductivity. In the inset of Fig. 6, it can be seen the rubber composite can light up a LED device with blue light. Therefore, the xSBR rubber can transfer from insulator into semiconducting materials by incorporation of the conductive PPy@HNTs.

3.4. Mechanical properties of the xSBR/PPy@HNTs composites

HNTs show high aspect ratios and high strength (about 130 GPa of the elastic modulus). The PPy@HNTs can be uniformly dispersed in the xSBR matrix as seen from the SEM result. The influence of PPy@HNTs on the mechanical properties of xSBR was investigated. Fig. 7(a) shows the stress-strain curves of xSBR/PPy@HNTs composites. Table 1 summarizes the data of the mechanical properties. The tensile strength of the composites increases with the filler loading. When the filler content is 10 wt%, the tensile strength of

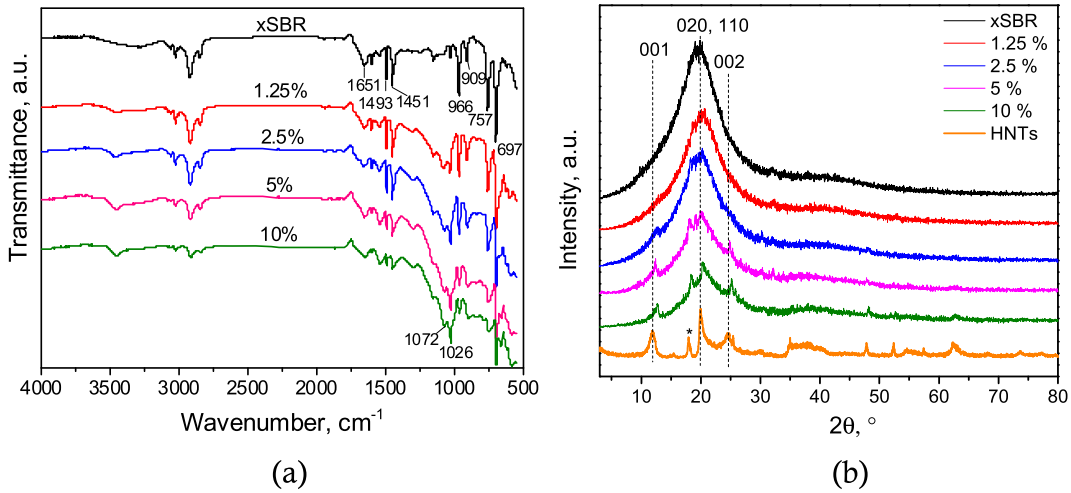

Fig. 4. FTIR spectra of xSBR and xSBR/PPy@HNTs composite (a); XRD patterns of xSBR, HNTs, and xSBR/PPy@HNTs composite (b). * in the HNTs pattern refer to the peaks of impurities in the HNTs.

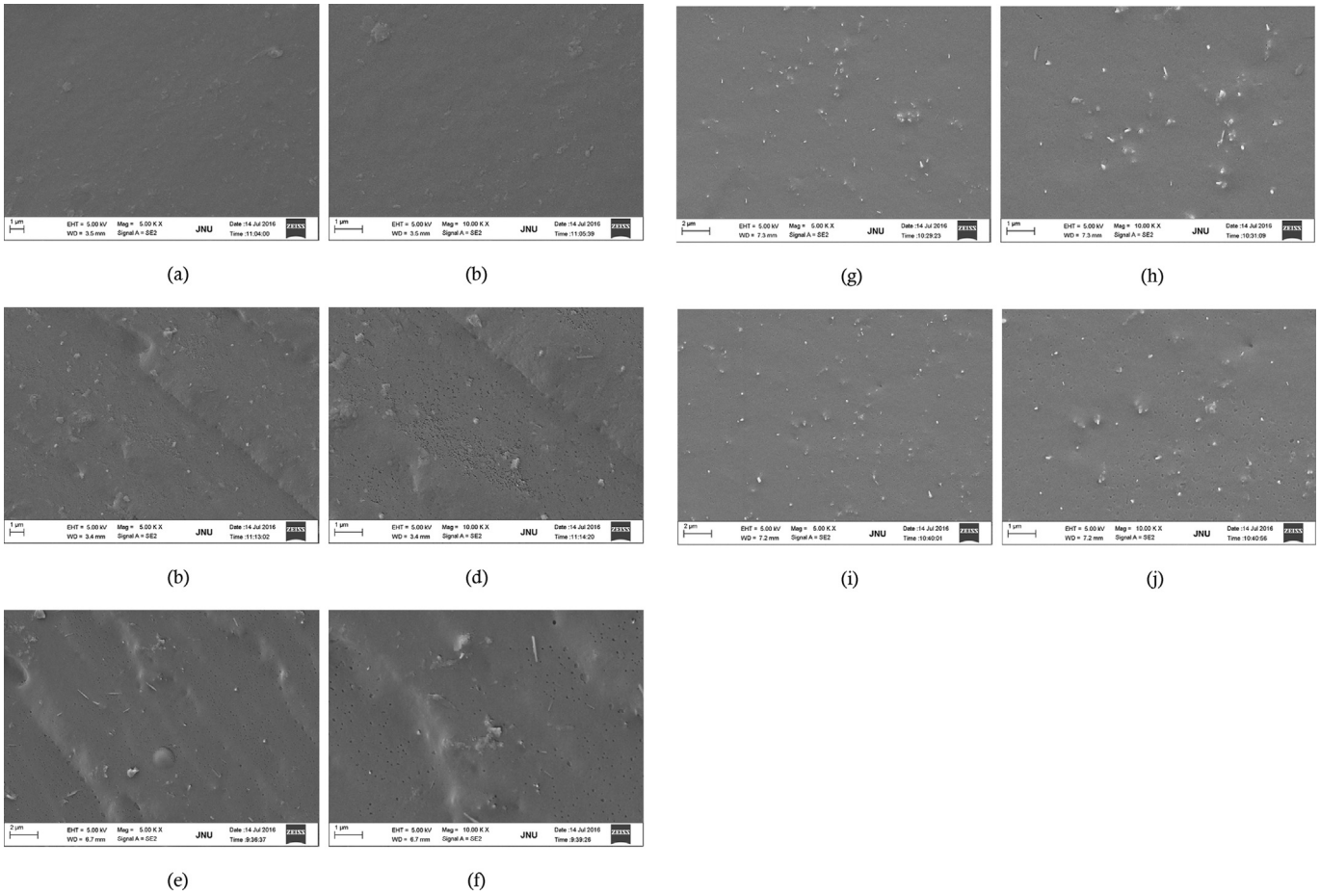

Fig. 5. SEM images of xSBR/PPy@HNTs composite: (a) and (b) xSBR; (c) and (d) 1.25%; (e) and (f) 2.5%; (g) and (h) 5%; (i) and (j) 10%.

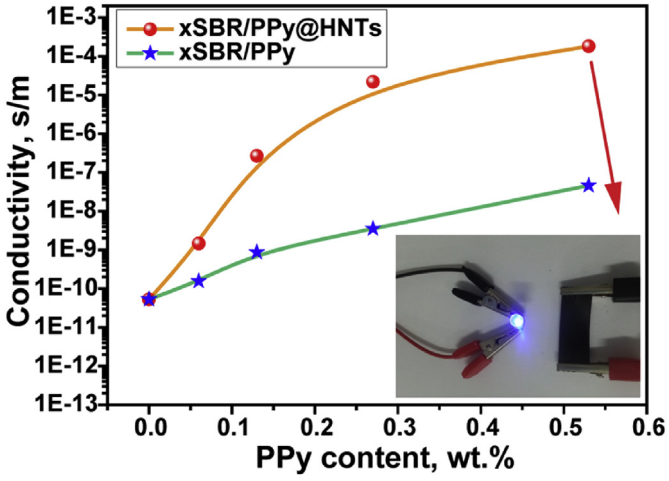

Fig. 6. Conductivity of the xSBR/PPy@HNTs and xSBR/PPy composites (inset show the xSBR/PPy@HNTs (10%) composite can light up a LED device).

the composite is 3.75 MPa which is 1.1 multiples of the neat xSBR. When the content of filler is less than 1.25 wt%, both the tensile strength and the elongation at break of the composites are improved simultaneously. With further increasing filler loading (beyond 2.5 wt%), the tensile strength of the xSBR/PPy@HNTs composites continues to increase, while the elongation at break slightly decreases. This phenomenon can be attributed to the formation of a rigid network in the rubber matrix with relatively high filler loading. The rigid filler network will stiffen the composite and inhibit the flexibility of the rubber chain. From Table 1, the tensile modulus at 100%, 300%, and 500% strain of the composites is also gradually increases with the increase of PPy@HNTs content (expect the tensile modulus at 100% for 1.25% PPy@HNTs content). For example, the modulus at 500% strain of xSBR/PPy@HNTs composites with 5 wt% filler content is 3.17 MPa, which is 2.07 multiples of the neat xSBR. The improvement of the tensile properties is attributed to the uniform dispersion of the PPy@HNTs and the good interfacial interactions between PPy@HNTs and rubber. Although the organic layer of PPy on HNTs is thin and the grafting ratio is low, it is supposed that both PPy and HNTs can interact with the polar xSBR via hydrogen bond interactions [32]. So, even if PPy can not fully wrapped the tubes, the interfacial bonding of the xSBR/PPy@HNTs composite is satisfy and is responsible for the enhancement of the properties. Without HNTs template, neat PPy can also reinforce the xSBR composites but at a relatively low level. This is related to the poor dispersion state and weak reinforcing ability of the PPy in rubber matrix [15].

To better understand the change of mechanical properties of the rubber composite, the data are recast in in the form of a reduced stress, σ^*, versus reciprocal extension ratio,$1/\lambda$, using the Mooney-Rivlin equation (Fig. 7(b)) [42]. The equation is given as follows:

$$\sigma^* = \sigma/(\lambda - \lambda^{-2}) = 2C_1 + 2C_2\lambda^{-1}$$

where σ is the true stress, $2C_1$ and $2C_2$ are constants, $\lambda = L/$

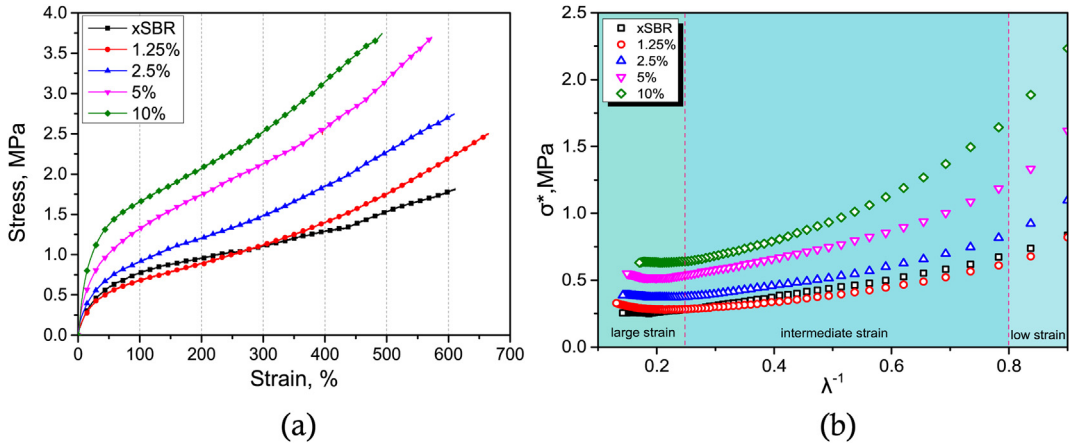

Fig. 7. Tensile stress-strain curves of xSBR/PPy@HNTs composite (a); σ* as a function of λ^{-1} of xSBR/PPy@HNTs composite based on the Mooney–Rivlin equation (b).

Table 1
The mechanical properties of xSBR/PPy@HNTs and xSBR/PPy composites (data in parentheses represent standard deviation).

Samples		Modulus at 100% strain (MPa)	Modulus at 300% strain (MPa)	Modulus at 500% strain (MPa)	Tensile strength (MPa)	Elongation at break (%)
Neat xSBR		0.78 (0.04)	1.10 (0.01)	1.53 (0.04)	1.81 (0.14)	611.0 (25.0)
PPy@HNTs content (%)	1.25	0.68 (0.04)	1.12 (0.10)	1.75 (0.15)	2.50 (0.21)	665.0 (35.2)
	2.5	0.91 (0.08)	1.48 (0.07)	2.27 (0.08)	2.74 (0.14)	609.7 (24.8)
	5	1.32 (0.09)	2.13 (0.14)	3.17 (0.11)	3.70 (0.18)	573.0 (22.0)
	10	1.65 (0.10)	2.53 (0.07)	–	3.75 (0.20)	492.5 (10.3)
PPy content (%)	0.06	0.87 (0.13)	1.71 (0.07)	–	2.01 (0.55)	342.9 (73.7)
	0.13	1.13 (0.06)	2.30 (0.01)	–	2.92 (0.60)	367.5 (27.5)
	0.27	0.98 (0.08)	2.16 (0.13)	–	2.38 (0.15)	324.5 (21.0)
	0.53	1.45 (0.09)	–	–	2.71 (0.21)	212.0 (15.2)

$L_0 = 1 + \varepsilon$, and L and L_0 are the final and initial lengths, and ε is the tensile strain.

As shown in Fig. 7(b), the Mooneye-Rivlin plots can be divided into the three regions of strain: lows train ($1/\lambda > 0.8$), intermediate strain ($1/\lambda$ = ~0.25–0.8) and high strain ($1/\lambda < 0.25$) [42]. It can be seen that the σ* of composites is higher than that of neat xSBR (expect the curve in the intermediate and low strain of xSBR/PPy@HNTs composites with 1.25 wt% filler content, which can be attributed to the softening effect of rubber by incorporation of small quantity of HNTs). The increased σ* of composite in the high strain region is due to the reinforcement or a "strain amplification" effect during the stretching process, as expected for the rigid tubular-like filler. This result also implies a strong interface in xSBR/PPy@HNTs composites, which are benefit for the chain orientation between neighboring nanoparticles when a large deformation is applied. The similar reinforcement effects of HNTs towards rubbers have also been found [43–46].

The influence of PPy@HNTs on dynamic properties of xSBR was further studied by DMA (Fig. 8). The storage modulus (E') and loss tangent (tan δ) of xSBR/PPy@HNTs composites are plotted as a function of temperature. Table 2 summarized the values of E′ at −100, 30, and 70 °C and peak values and peak temperature of tan δ for xSBR/PPy@HNTs composites. E′ of xSBR/PPy@HNTs composites increases with the increase of filler content both in rubber state and glass state. The increase trend is especially significant at the rubber state after glass transition. Storage modulus at 30 °C of xSBR/PPy@HNTs composites with 10% filler content is 96.08 MPa which is 7.6 multiple of that of neat xSBR. This DMA result is consistent with the results of the static tensile test. The E′ of the composite is mainly affected by the fillers network in the polymer matrix. As the filler loading increases, a more perfect network within the polymer matrix is formed, which result in effective load transfer of the rubber matrix to the fillers and consequently the improvement of the storage modulus. With the increase of filler loading, the peak value of tan δ decreases from 0.95 of neat xSBR to 0.70 of the composite with 10% PPy@HNTs content. The decrease of the peak value of the tan δ curve is related to the decrease of the rubber matrix material content, which suggests the decrease of the damping performance by the incorporation of modified HNTs. The decrease of the peak also indicates that the rubber molecular chain in the composites is absorbed and trapped on the surface of the nanotubes, which limits the flexibility and mobility of the rubber macromolecular chains. The peak temperature of the tan δ curve corresponds to the T_g of the polymer. It can be seen that the T_g decreases from 28.55 °C to 23.22 °C with the increase of the filler loading. A shift of the T_g to lower temperature has also been found in the SBR/silica composite [47,48]. Previous study showed that the favorable interfacial interactions of the organophilic filler with non-polar rubber chains leaded to a decrease in T_g when an organophilic filler was present in rubber composite [48]. For the present systems, the raw HNTs was treated by the organophilic PPy, which contributed to the decrease of the T_g.

3.5. Thermal properties of the xSBR/PPy@HNTs composites

DSC and TGA experiment were performed to investigate the influence of PPy@HNTs on the thermal properties of the xSBR. Fig. 9(a) shows the DSC heating curves for the xSBR/PPy@HNTs composites with different filler contents. Different from the DMA result, all the composites show T_g in the range of 10.3–12.1 °C which are sustainably lower than those determined by DMA testing. This arises the different principle for determining T_g for the

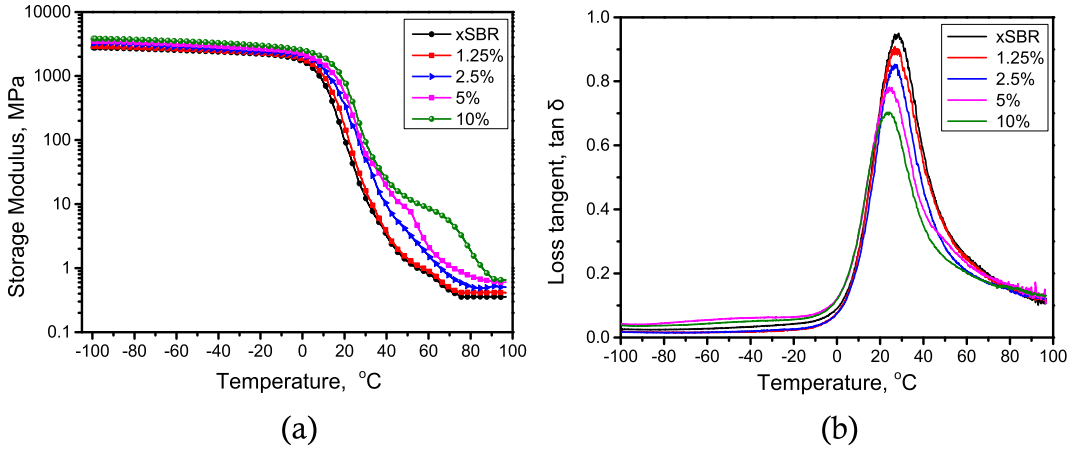

Fig. 8. The temperature dependence of the storage modulus E′ for xSBR/PPy@HNTs composites with various PPy@HNTs contents (a); the temperature dependence of the loss tangent tan δ for xSBR/PPy@HNTs composites with various PPy@HNTs contents (b).

Table 2
The data of storage modulus at different temperature, tan δ peak value, and tan δ peak temperature for xSBR/PPy@HNTs composites.

PPy@HNTs content (%)	Storage modulus at −100 °C (MPa)	Storage modulus at 30 °C (MPa)	Storage modulus at 70 °C (MPa)	tan δ peak values (−)	tan δ peak temperature (°C)
0	2780.33	12.65	0.45	0.95	28.55
1.25	2903.91	16.99	0.50	0.91	26.78
2.5	3300.10	50.03	0.75	0.85	26.65
5	3504.53	62.23	1.08	0.78	24.34
10	3842.32	96.08	5.34	0.70	23.22

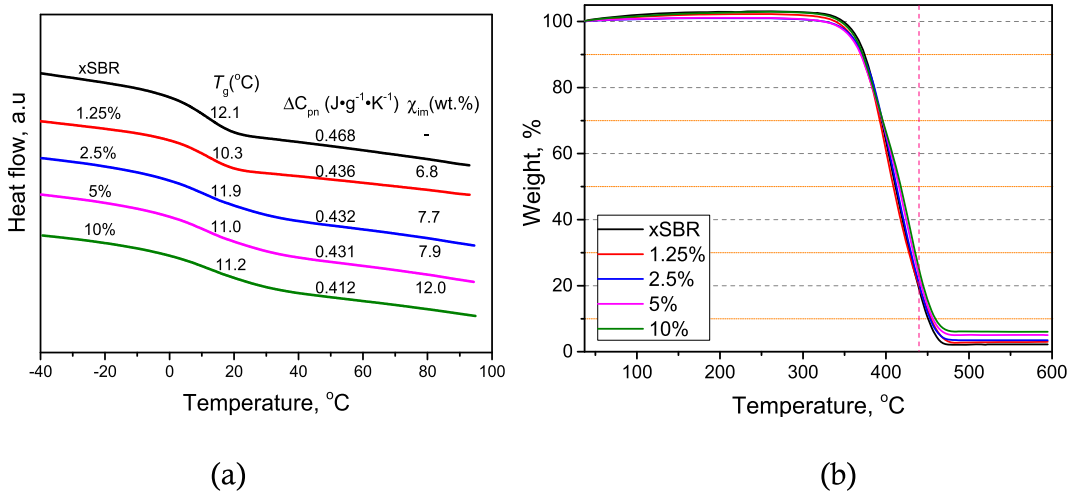

Fig. 9. DSC heating curves of xSBR/PPy@HNTs composites with various PPy@HNTs contents (a); TGA curves of xSBR/PPy@HNTs composites with various PPy@HNTs contents (b).

two methods. The DMA method measures the hysteresis between the applied force and the response of the macromolecular chain under repeated small amplitude strain cycles. While the DSC method measures the enthalpy change during heating or cooling [49]. The T_g of the rubber composites is also lower than that of neat xSBR (expect for that of composite with 2.5 wt%). To evaluate the amount of immobilized rubber around the PPy@HNTs in the composite, the value of χ_{im} (the weight fraction of the immobilized polymer layer) was calculated by DSC data. Compared to pure xSBR, ΔC_{pn} shows a systematic decrease trend with the increase of PPy@HNTs loading, indicating that part of fillers in the composites does not participate in the glass transition behavior of the polymer bulk. With the content of filler increases, the value of χ_{im} gradually increases from 6.8% to 12.0%, suggesting that more and more rubber molecule chains are immobilized by fillers.

Fig. 9(b) compares the decomposition behavior of xSBR and xSBR/PPy@HNTs composites. The temperature corresponding to the maximum weight loss of xSBR is near 405 °C. The TG curves of all the composites do not show regularity when the temperature is less than 450 °C, and the curves almost coincide for all the samples. However, when the temperature is higher than 440 °C, the curves of the composite are above that of neat xSBR with the increase in the filler content. This suggests that the thermal stability of xSBR slightly increases at high temperature region by the addition of PPy@HNTs. At 600 °C, the residual weight of the composites increases with the increase of filler loading.

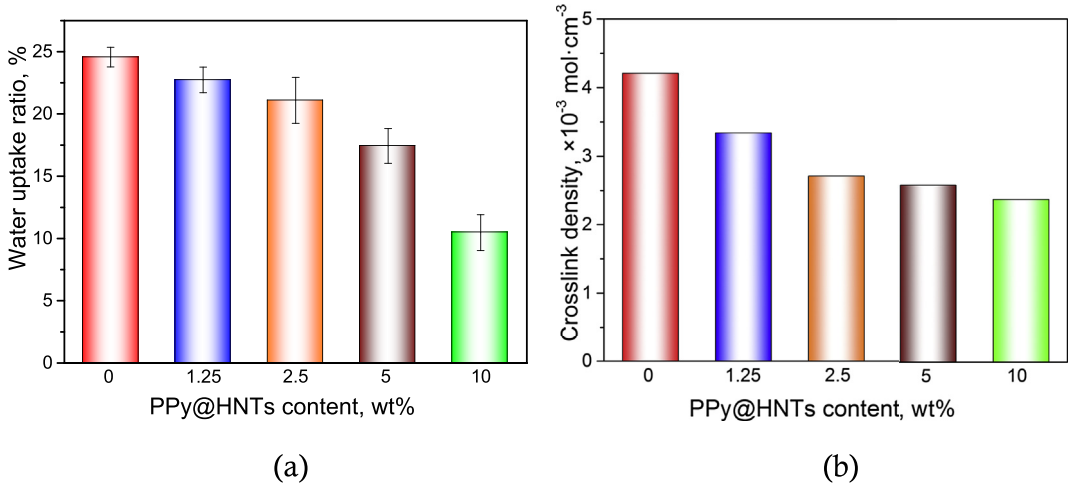

Fig. 10. Water uptake ratio of xSBR/PPy@HNTs composites (a); crosslink density of xSBR/PPy@HNTs composite (b).

3.6. Swelling properties of the xSBR/PPy@HNTs composites

Fig. 10(a) shows the water absorption ratio of the xSBR/PPy@HNTs composites for 3 days. The water absorption ratio of composites decreases from 24.6% to 10.5% with the increase of the filler loading, which is related to the formation of rigid network in the composites which limits the movement of the rubber molecular chain. Fig. 10(b) shows the influence of PPy@HNTs loading on the crosslink density of xSBR. Though our system is not crosslinked, the crosslinking density can be compared to study whether there are interactions between xSBR and PPy@HNTs. It is generally considered that the nanoparticles can adsorbed the rubber chains, which leads to the decrease of the crosslink density. It can be seen that the crosslink density of the composite decreases with the increase of the filler content, which is attributed to the high specific surface areas of PPy@HNTs. The surface adsorption effect of HNTs result in a barrier effect for the formation of physical crosslinking points via macromolecular chain tangles [50]. Previous report also found that the addition of inorganic filler reduced the volume fraction of rubber and hindered the curing, leading to the decrease of crosslinked rubber density [51].

4. Conclusions

In summary, PPy@HNTs conductive filler was prepared by adding ferric chloride as oxidizing agent in a uniformly dispersed HNTs and pyrrole aqueous dispersion. ζ-potential measurement, FTIR, and TEM showed that PPy was successfully polymerized on the surfaces of the nanotubes, leading to a continuous conductive layer on HNTs. xSBR/PPy@HNTs composite films were prepared via solution mixing and casting drying method. The incorporation of the conductive filler PPy@HNTs successfully conferred the good conductivity of xSBR. When the content of filler was 10%, the conductivity of the sample was 1.82×10^{-4} s/m. FTIR and XRD confirmed the interfacial interactions between the PPy@HNTs and the xSBR. PPy@HNTs could be uniformly dispersed in the rubber matrix and nearly no aggregates of PPy@HNTs could be found. Both the tensile strength and the elongation at break of the rubber composites were improved by the addition of PPy@HNTs. Effective load transfer of the rubber matrix to the fillers leaded to the improvement of the storage modulus. A slightly decreased glass transition temperature of the composite was found. The thermal stability of xSBR slightly increased at high temperature region by the addition of PPy@HNTs. PPy@HNTs leaded to reduced water absorption and crosslinking density of the xSBR. All results showed that the addition of PPy@HNTs could improve both the electrical conductivity and mechanical performance of the rubber composites.

Acknowledgments

This work was supported by the National High Technology Research and Development Program of China (grant numbers 2015AA020915), the National Natural Science Foundation of China (grant numbers 51473069, 51502113), and the Guangdong Natural Science Funds for Distinguished Young Scholar (grant numbers S2013050014606), Science and Technology Planning Project of Guangdong Province (grant numbers 2014A020217006), Guangdong Special Support Program (grant numbers 2014TQ01C127), and the Pearl River S&T Nova Program of Guangzhou (grant numbers 201610010026).

References

[1] X. Wu, C. Lu, Y. Han, Z. Zhou, G. Yuan, X. Zhang, Cellulose nanowhisker modulated 3D hierarchical conductive structure of carbon black/natural rubber nanocomposites for liquid and strain sensing application, Compos. Sci. Technol. 124 (2016) 44–51.
[2] X. Wu, Y. Han, X. Zhang, C. Lu, Highly sensitive, stretchable, and wash-durable strain sensor based on ultrathin conductive layer@ polyurethane yarn for tiny motion monitoring, ACS Appl. Mater. Interfaces 8 (15) (2016) 9936–9945.
[3] N. George, J. Chandra, A. Mathiazhagan, R. Joseph, High performance natural rubber composites with conductive segregated network of multiwalled carbon nanotubes, Compos. Sci. Technol. 116 (2015) 33–40.
[4] L. Li, F. Yan, G. Xue, Preparation of a porous conducting polymer film by electrochemical synthesis–solvent extraction method, J. Appl. Polym. Sci. 91 (1) (2004) 303–307.
[5] S.Y. Liew, W. Thielemans, D.A. Walsh, Electrochemical capacitance of nanocomposite polypyrrole/cellulose films, J. Phys. Chem. C 114 (41) (2010) 17926–17933.
[6] Z. Wang, P. Tammela, P. Zhang, J. Huo, F. Ericson, M. Strømme, L. Nyholm, Freestanding nanocellulose-composite fibre reinforced 3D polypyrrole electrodes for energy storage applications, Nanoscale 6 (21) (2014) 13068–13075.
[7] X. Wu, V.L. Chabot, B.K. Kim, A. Yu, R.M. Berry, K.C. Tam, Cost-effective and scalable chemical synthesis of conductive cellulose nanocrystals for high-performance supercapacitors, Electrochim. Acta 138 (2014) 139–147.
[8] X. Wu, J. Tang, Y. Duan, A. Yu, R.M. Berry, K.C. Tam, Conductive cellulose nanocrystals with high cycling stability for supercapacitor applications, J. Mater. Chem. A 2 (45) (2014) 19268–19274.
[9] B. Weng, R. Shepherd, J. Chen, G.G. Wallace, Gemini surfactant doped polypyrrole nanodispersions: an inkjet printable formulation, J. Mater. Chem. 21 (6) (2011) 1918–1924.
[10] F. Yan, G. Xue, F. Wan, A flexible giant magnetoresistance sensor prepared completely by electrochemical synthesis, J. Mater. Chem. 12 (9) (2002) 2606–2608.

[11] T.Y.V. Vernitskaya, O.N. Efimov, Polypyrrole: a conducting polymer; its synthesis, properties and applications, Russ. Chem. Rev. 66 (5) (1997) 443–457.
[12] L. Zhang, T. Wang, P. Liu, Polyaniline-coated halloysite nanotubes via in-situ chemical polymerization, Appl. Surf. Sci. 255 (5) (2008) 2091–2097.
[13] C. Yuan, J. Li, L. Hou, X. Zhang, L. Shen, X.W.D. Lou, Ultrathin mesoporous NiCo2O4 nanosheets supported on Ni foam as advanced electrodes for supercapacitors, Adv. Funct. Mater. 22 (21) (2012) 4592–4597.
[14] L. Jin, Z.-Q. Feng, M.-L. Zhu, T. Wang, M.K. Leach, Q. Jiang, A novel fluffy conductive polypyrrole nano-layer coated PLLA fibrous scaffold for nerve tissue engineering, J. Biomed. Nanotechnol. 8 (5) (2012) 779–785.
[15] X. Zhang, X. Wu, C. Lu, Z. Zhou, Dialysis-free and in situ doping synthesis of polypyrrole@ cellulose nanowhiskers nanohybrid for preparation of conductive nanocomposites with enhanced properties, ACS Sustain. Chem. Eng. 3 (4) (2015) 675–682.
[16] X. Wu, C. Lu, H. Xu, X. Zhang, Z. Zhou, Biotemplate synthesis of polyaniline@ cellulose nanowhiskers/natural rubber nanocomposites with 3D hierarchical multiscale structure and improved electrical conductivity, ACS Appl. Mater. Interfaces 6 (23) (2014) 21078–21085.
[17] M. Du, B. Guo, D. Jia, Thermal stability and flame retardant effects of halloysite nanotubes on poly (propylene), Eur. Polym. J. 42 (6) (2006) 1362–1369.
[18] B. Huang, M. Liu, Z. Long, Y. Shen, C. Zhou, Effects of halloysite nanotubes on physical properties and cytocompatibility of alginate composite hydrogels, Mater. Sci. Eng. C 70 (2017) 303–310.
[19] E. Joussein, S. Petit, J. Churchman, B. Theng, D. Righi, B. Delvaux, Halloysite clay minerals–a review, Clay Min. 40 (4) (2005) 383–426.
[20] Y. Ye, H. Chen, J. Wu, C.M. Chan, Interlaminar properties of carbon fiber composites with halloysite nanotube-toughened epoxy matrix, Compos. Sci. Technol. 71 (5) (2011) 717–723.
[21] S. Guggenheim, R.A. Eggleton, Crystal chemistry, classification, and identification of modulated layer silicates, Rev. Mineral. Geochem 19 (1) (1988) 675–725.
[22] Y. Lvov, E. Abdullayev, Functional polymer–clay nanotube composites with sustained release of chemical agents, Prog. Polym. Sci. 38 (10) (2013) 1690–1719.
[23] D. Lu, H. Chen, J. Wu, C.M. Chan, Direct measurements of the Young's modulus of a single halloysite nanotube using a transmission electron microscope with a bending stage, J. Nanosci. Nanotechnol. 11 (9) (2011) 7789–7793.
[24] G. Nyström, A. Mihranyan, A. Razaq, T. Lindström, L. Nyholm, M. Strømme, A nanocellulose polypyrrole composite based on microfibrillated cellulose from wood, J. Phys. Chem. B 114 (12) (2010) 4178–4182.
[25] X. Zeng, Z. Sun, H. Wang, Q. Wang, Y. Yang, Supramolecular gel composites reinforced by using halloysite nanotubes loading with in-situ formed Fe_3O_4 nanoparticles and used for dye adsorption, Compos. Sci. Technol. 122 (2016) 149–154.
[26] M. Liu, Z. Jia, D. Jia, C. Zhou, Recent advance in research on halloysite nanotubes-polymer nanocomposite, Prog. Polym. Sci. 39 (8) (2014) 1498–1525.
[27] E. Abdullayev, Y. Lvov, Halloysite clay nanotubes as a ceramic "skeleton" for functional biopolymer composites with sustained drug release, J. Med. Chem. B 1 (23) (2013) 2894–2903.
[28] M. Du, B. Guo, D. Jia, Newly emerging applications of halloysite nanotubes: a review, Polym. Int. 59 (5) (2010) 574–582.
[29] M. Du, B. Guo, M. Liu, D. Jia, Formation of reinforcing inorganic network in polymer via hydrogen bonding self-assembly process, Polym. J. 39 (3) (2007) 208–212.
[30] M. Liu, B. Guo, M. Du, X. Cai, D. Jia, Properties of halloysite nanotube–epoxy resin hybrids and the interfacial reactions in the systems, Nanotechnology 18 (45) (2007) 455703.
[31] C. Yang, P. Liu, Y. Zhao, Preparation and characterization of coaxial halloysite/polypyrrole tubular nanocomposites for electrochemical energy storage, Electrochim. Acta 55 (22) (2010) 6857–6864.
[32] M. Du, B. Guo, Y. Lei, M. Liu, D. Jia, Carboxylated butadiene–styrene rubber/halloysite nanotube nanocomposites: interfacial interaction and performance, Polymer 49 (22) (2008) 4871–4876.
[33] P.J. Flory, J. Rehner Jr., Statistical mechanics of cross-linked polymer networks I. Rubberlike elasticity, J. Chem. Phys. 11 (11) (1943) 512–520.
[34] P.J. Flory, Statistical mechanics of swelling of network structures, J. Chem. Phys. 18 (1) (1950) 108–111.
[35] M. Liu, Y. Zhang, C. Wu, S. Xiong, C. Zhou, Chitosan/halloysite nanotubes bionanocomposites: structure, mechanical properties and biocompatibility, Int. J. Biol. Macromol. 51 (4) (2012) 566–575.
[36] J. Madejová, FTIR techniques in clay mineral studies, Vib. Spectrosc. 31 (1) (2003) 1–10.
[37] J. Wu, Q. Li, L. Fan, Z. Lan, P. Li, J. Lin, S. Hao, High-performance polypyrrole nanoparticles counter electrode for dye-sensitized solar cells, J. Power Sources 181 (1) (2008) 172–176.
[38] T. Bein, P. Enzel, Encapsulation of polypyrrole chains in zeolite channels, Angew. Chem. Int. Ed. Engl. 28 (12) (1989) 1692–1694.
[39] M. De Sarkar, P. De, A. Bhowmick, Diimide reduction of carboxylated styrene–butadiene rubber in latex stage, Polymer 41 (3) (2000) 907–915.
[40] R. Rong, X. Xu, S. Zhu, B. Li, X. Wang, K. Tang, Facile preparation of homogeneous and length controllable halloysite nanotubes by ultrasonic scission and uniform viscosity centrifugation, Chem. Eng. J. 291 (2016) 20–29.
[41] T. Pojanavaraphan, R. Magaraphan, Fabrication and characterization of new semiconducting nanomaterials composed of natural layered silicates (Na+-MMT), natural rubber (NR), and polypyrrole (PPy), Polymer 51 (5) (2010) 1111–1123.
[42] S. Peddini, C. Bosnyak, N. Henderson, C. Ellison, D. Paul, Nanocomposites from styrene–butadiene rubber (SBR) and multiwall carbon nanotubes (MWCNT) part 2: mechanical properties, Polymer 56 (2015) 443–451.
[43] Z.-x. Jia, Y.-f. Luo, S.-y. Yang, B.-c. Guo, M.-l. Du, D.-m. Jia, Morphology, interfacial interaction and properties of styrene-butadiene Rubber/Modified halloysite nanotube nanocomposites, Chin. J. Polym. Sci. 27 (06) (2009) 857–864.
[44] S. Rooj, A. Das, V. Thakur, R. Mahaling, A.K. Bhowmick, G. Heinrich, Preparation and properties of natural nanocomposites based on natural rubber and naturally occurring halloysite nanotubes, Mater. Des. 31 (4) (2010) 2151–2156.
[45] P. Pasbakhsh, H. Ismail, M.A. Fauzi, A.A. Bakar, EPDM/modified halloysite nanocomposites, Appl. Clay Sci. 48 (3) (2010) 405–413.
[46] B. Guo, F. Chen, Y. Lei, X. Liu, J. Wan, D. Jia, Styrene-butadiene rubber/halloysite nanotubes nanocomposites modified by sorbic acid, Appl. Surf. Sci. 255 (16) (2009) 7329–7336.
[47] P. Mélé, S. Marceau, D. Brown, Y. de Puydt, N.D. Albérola, Reinforcement effects in fractal-structure-filled rubber, Polymer 43 (20) (2002) 5577–5586.
[48] V. Arrighi, I.J. McEwen, H. Qian, M.B. Serrano Prieto, The glass transition and interfacial layer in styrene-butadiene rubber containing silica nanofiller, Polymer 44 (20) (2003) 6259–6266.
[49] M. Liu, Q. Peng, B. Luo, C. Zhou, The improvement of mechanical performance and water-response of carboxylated SBR by chitin nanocrystals, Eur. Polym. J. 68 (2015) 190–206.
[50] A. Mousa, J. Karger-Kocsis, Rheological and thermodynamical behavior of styrene/butadiene rubber-organoclay nanocomposites, Macromol. Mater. Eng. 286 (4) (2001) 260–266.
[51] R. Stephen, C. Ranganathaiah, S. Varghese, K. Joseph, S. Thomas, Gas transport through nano and micro composites of natural rubber (NR) and their blends with carboxylated styrene butadiene rubber (XSBR) latex membranes, Polymer 47 (3) (2006) 858–870.